Performance of the JWST/MIRI Si:As detectors

Michael E. Ressler[a], Hyung Cho[a], Richard A. M. Lee[a], Kalyani G. Sukhatme[a], John J. Drab[b], George Domingo[c], Mark E. McKelvey[d], Robert E. McMurray, Jr.[d], and Jessie L. Dotson[d]

[a]Jet Propulsion Laboratory, California Institute of Technology,
4800 Oak Grove Drive, Pasadena, CA, 91109, USA;
[b]Raytheon Vision Systems, Building B2 / Mail Stop 8,
75 Coromar Drive, Goleta, CA, 93117, USA;
[c]Domingo Engineering, 2116 Softwind Lane, Encinitas, CA, 92024, USA;
[d]NASA Ames Research Center, M/S 244-10, Moffett Field, CA, 94035, USA

ABSTRACT

The Mid-Infrared Instrument (MIRI) is a 5 to 28 micron imager and spectrometer that is slated to fly aboard the JWST in 2013. Each of the flight arrays is a 1024×1024 pixel Si:As impurity band conductor detector array, developed by Raytheon Vision Systems. JPL, in conjunction with the MIRI science team, has selected the three flight arrays along with their spares. We briefly summarize the development of these devices, then describe the measured performance of the flight arrays along with supplemental data from sister flight-like parts.

Keywords: Infrared detectors, arsenic-doped silicon, JWST, MIRI

1. INTRODUCTION

The JWST Mid-Infrared Instrument (MIRI) is a combination imager, coronagraph, and spectrometer that functions over the 5 to 28 micrometer wavelength range [1,2]. MIRI contributes significantly to all four of the primary JWST science themes, so its success is critical to the overall success of the JWST mission. To best implement the optical design of MIRI, the imager, coronagraph, and a low-resolution grism spectrometer are combined onto one focal plane, while a medium resolution, integral field unit (IFU) spectrometer is split onto two separate focal planes. We therefore require three mid-infrared detector arrays with a suitably large format and very sensitive performance characteristics to take full advantage of the platform provided by the JWST observatory. For brevity, we refer to these detectors/channels as "IC" for the imager/coronagraph channel, "SW" for the short wavelength half of the IFU spectrometer, and "LW" for the long wavelength half of the spectrometer.

The detector arrays are attached to a fanout board, mounting structure, and ribbon cable; this assembly is the "Detector Assembly" (DA) and represents the final deliverable unit from the detector vendor (see Figure 1). At JPL, these DAs are installed into a housing assembly known as a "Focal Plane Module" (FPM, see [3] for further details). After extensive qualification and characterization, the FPMs are attached to the MIRI Optical Module.

2. DEVICE DESCRIPTION & HISTORY

The detector arrays needed for MIRI are 1024×1024 pixel arsenic-doped silicon (Si:As) hybrid arrays. The million pixels are required to produce adequate sampling on the wide fields afforded by the telescope, and the chosen detector material is by far the most mature for this wavelength range. Raytheon Vision Systems (RVS) of Goleta, CA, was competitively selected in May 2003 to provide the detectors for MIRI. Although the MIRI detectors (more properly called Sensor Chip Assemblies, or SCAs) are very closely related to the 256×256 pixel Si:As arrays currently flying in the IRAC instrument aboard the Spitzer Space Telescope [4], the 16× increase in the number of pixels, the tighter sensitivity requirements, and the simple fact that the Spitzer SCAs were produced more than 10 years ago necessitated a lengthy development process to ensure high performing detectors for MIRI.

Send correspondence to M.E.R.: E-mail: Michael.E.Ressler@jpl.nasa.gov, Telephone: 1 818 354 5576

High Energy, Optical, and Infrared Detectors for Astronomy III, edited by David A. Dorn, Andrew D. Holland,
Proc. of SPIE Vol. 7021, 70210O, (2008) · 0277-786X/08/$18 · doi: 10.1117/12.789606

The first megapixel class readout developed by RVS was the SB-226 readout in 2000, followed by a second generation SB-291 in 2002 [5]. Neither of these readouts would have met the MIRI requirements; however, the MIRI project was able to learn from issues found during these development programs, and all were addressed during the first MIRI build.

The readouts for MIRI were also produced in two generations. The engineering version SB-305 was mostly successful, but there were still issues with noise performance and multiplexer glow that needed to be addressed. The flight version SB-375 readout was then finalized, and it is has been successfully operated. This design has 1024×1024 pixels on a 25 micrometer pitch, four data outputs, reference pixels at the "left" and "right" edges of the array, and a 5th dedicated reference output [6].

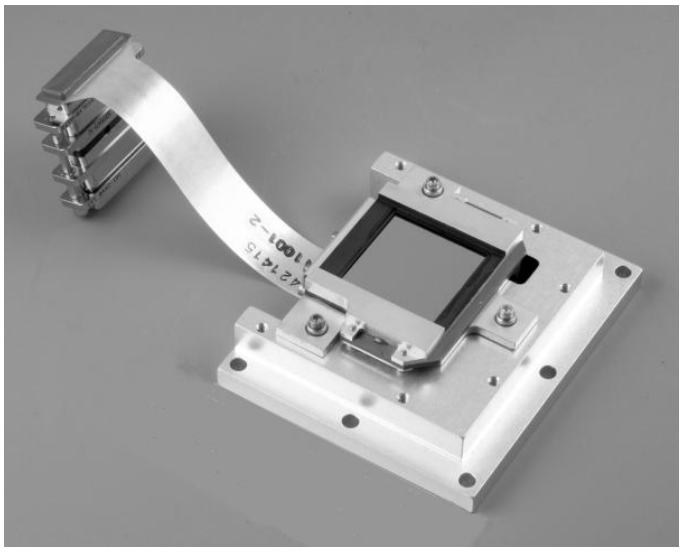

Figure 1. A picture of a Detector Assembly, the deliverable from Raytheon Vision Systems. The DA consists of the SCA, a baffle shield around the SCA, a small fanout board, a mounting pedestal, and a cable. It is shown here mounted on an aluminum test fixture.

Detector layer purity was also highlighted as a key issue, and steps were put into place to ensure the cleanest possible detector growth. Two flavors of detector were produced: a "baseline" detector with a thicker and more highly doped active layer whose intent was to meet all requirements without question, but would require very good purity in order to be functional, and a "contingency" detector with a thinner, lower doped active layer that would possibly not quite meet all the requirements, but would still function as a reasonable detector if the purity could not be improved [6].

The basic readout mode for the MIRI detectors is a simple sample-up-the-ramp pattern as this provides the best sensitivity for a mixture of observing conditions [7]. Because MIRI is able to send almost all of its data to the ground, this method has the advantage that the raw data is available if alternate processing is desired, and the appropriate frames can be selected from all those available. For MIRI, a "frame" is a single clocking scan through the array; an "integration" is a number of non-destructive readout frames where photons are allowed to integrate (there is no "dead" time between frames; therefore, the integration length is an integer times the frame time); and an "exposure" is a number of sequential integrations to be performed before the next software command is received. These definitions fall into the JWST exposure paradigm, with the caveat that MIRI does not explicitly have "groups" of frames as the other instruments do. By definition, MIRI has one frame per group.

The performance requirements for the MIRI detectors are summarized in Table 1. The measured dark current, read noise, well depth, and linearity for the imager (IC) array were taken after the unit was fully assembled into a Focal Plane Module. Dark currents for the SW and LW arrays were obtained during SCA-level testing. The stability was measured on a qualification unit FPM that underwent far more cycles of cold functional testing than any of the flight FPMs will undergo. Finally, the latent image data was obtained with an older (flight detector layers, but with an SB-305 readout) engineering array, whose latent behavior should match the flight arrays.

3. EXPERIMENTAL SETUP

The MIRI detectors are tested in a two-channel dewar that has independent optical chains with only a liquid helium work surface in common. This allows us to test two devices simultaneously, each with their own optical source and filters. Each channel has a blackbody illumination source whose drive current is variable, allowing us to test over a range of fluxes. Each channel also has its own cold shield with light-tight seals in an effort to reduce the background to unmeasurable levels.

The blackbody sources consist of a current-driven emitter whose temperature is monitored. The temperature can be varied from approximately the LHe bath temperature up to 250 K. The blackbody temperature is stable in an open loop configuration and so does not require proportional-integral-differential (PID) temperature control.

Table 1. MIRI Detector Performance Requirements

Name	Value	IC	SW	LW
Min. Pixel Format	$> 1000 \times 1000$	1024×1024 active		
Pixel pitch	25 μm	25 μm by design		
Min. Integration Time	≤ 3 s	2.76 s typical		
Max. Integration Time	≥ 4000 s	Tested up to 5500 s		
Dark current	≤ 0.03 e^-/s at 6.7 K	0.17 e^-/s [a]	0.03 e^-/s [b]	0.17 e^-/s [a] [b]
Read Noise	< 19 e^- Fowler=8	14 e^-		
QE — IC, SW	> 0.5 (< 19 μm), > 0.38 (> 19 μm)	yes, see Figure 2	yes, see Figure 2	N/A
QE — LW	> 0.6 (12–27 μm)	N/A	N/A	yes, to 24 μm, see Figure 2
Full Well Capacity	$> 100{,}000$ e^-	$\geq 250{,}000$ e^-		
Latent Images	$< 2\%$ of primary	2.2% offset in next integration, much smaller slope (inferred flux) error		
Linearity	correctable to 0.25%	yes, see Figure 8 below		
Short/Long Term Stability	$< 0.5\%$	yes, see Figure 9 below		

Notes: a) The "baseline" detector material has about 6× higher dark current than the "contingency" material but, for the IC and LW channels, the sensitivity is limited by the various photon backgrounds rather than by the dark current noise or read noise. b) The noise on the SW and LW detectors has not yet been measured in our lowest noise testbed, but screening data show that the behavior should be similar to the IC array.

The optical path is contained entirely inside the dewar. External ports are available in the dewar but, in the MIRI test configuration, everything is contained within a shield that is heat sunk to the 4 K work surface. The sources produce a fairly uniform flux (to within 10%) on the detector surfaces except that an internal baffle produces a set of distinct Fresnel rings. Although at first deemed undesirable, these rings proved to be useful in later testing (especially for subarray readouts) due to their repeatability and predictability when modeled.

The temperature of the detectors is regulated to better than 1 mK in a closed-loop fashion using PID-type temperature controllers. The SCAs are mounted in a lead-less chip carrier (LCC) and have either a diode or resistive temperature sensor mounted in the LCC next to the SCA. In addition, the stage on which the LCC is mounted also has temperature sensors and heaters so that there are several ways the detector temperature can be monitored and controlled.

4. PERFORMANCE RESULTS

4.1 Quantum Yield

The quantum efficiency will be the chief contribution of the detectors to the instrument sensitivity for much of the MIRI wavelength range and operating modes. Most of the imaging functions and long wavelength spectrometer will be photon limited, either by Zodiacal light or by the JWST telescope background, so high responsivity is important. To help maximize the throughput, the three detectors are anti-reflection coated. The imager and SW arrays have coatings emphasizing the short wavelength range, 5–10 μm, while the LW array emphasizes the 12–20 μm range. The coatings, therefore, are designed to have reflectance minima at 6 and 16 μm, respectively.

The spectral quantum efficiency (more properly "quantum yield" in IBC devices, since we can only measure the quantum efficiency times the internal gain, ηG [8,9]) of the detectors cannot be measured trivially in detector array form, so we rely on measurements of test structures included on each wafer from which the flight detectors are selected.

Shown in Figure 2 is the measured curve for an uncoated test structure. The QE remains at roughly 50% QE over the range 8 to 23 μm. The other two curves are predictions of the effective QE with the two anti-reflection coatings we have chosen for the MIRI flight SCAs. With the "6-μm" coating, we expect 60% effective QE from 7 through 17 μm, while the "16-μm" coating will increase the QE to over 70% for the 14 to 22 μm range. We also expect a usable level of response at 28.22 μm to allow the detection of the molecular hydrogen 0–0 S(0) rotational line.

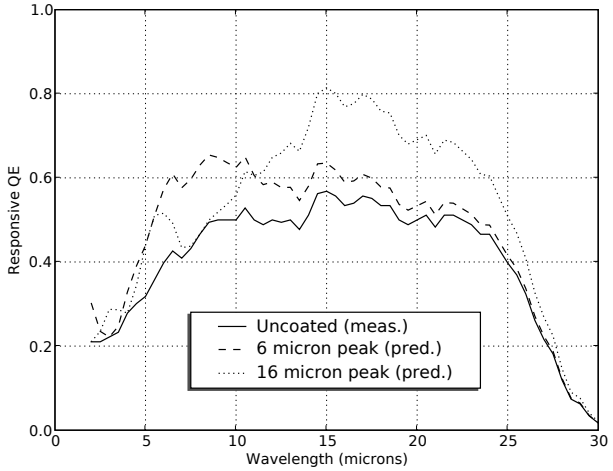

Figure 2. Quantum yield as measured and predicted in test structures from the same wafer as the flight detectors. The AR-coatings have reflection minima (peaks in transmission) at the indicated wavelengths. The detector bias voltage was 2 V, typical of the data obtained on the flight SCAs.

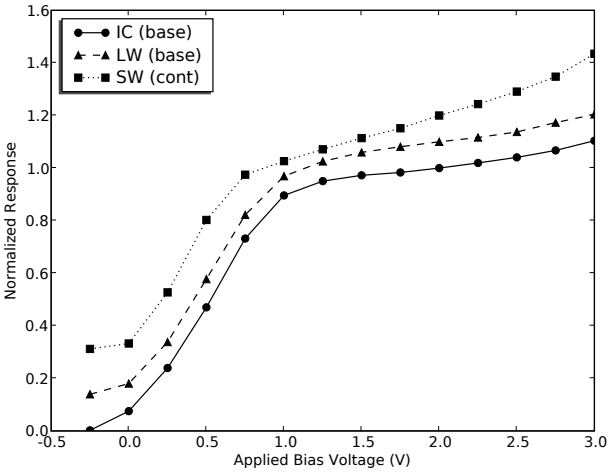

Figure 3. Response vs. applied bias voltage for each of the three flight detectors. All have been normalized to the value at 2.0 V applied bias, and the curves for the SW and LW arrays have then been offset for clarity.

4.2 Response vs. Bias Voltage

Finding the optimum bias voltage at which to run the detectors is a balance between maximizing the response vs. minimizing the dark current. While we have not yet done a full detective quantum efficiency (DQE) vs. bias plot, we have investigated the response vs. bias voltage. For both types of detectors, we see the classical "S-shaped" curve (Figure 3; both have a knee near 1.0 V). There are two characteristics to note: 1) zero applied bias still produces some photoresponse—there is an effective bias put on the unit cell capacitance from clock feedthrough of about 0.2 V; and 2) the baseline detectors have an inflection point near 2.0 V, while the contingency detector has one near 1.5 V. Generally speaking, this indicates the point of optimum bias but, because we have not completed the DQE study, we have chosen to do all the measurements reported here at 2.0 V applied bias.

4.3 Dark Current

The dark current performance of the detectors is especially critical as the short wavelength spectrometer channel will be detector limited. If the dark current can be kept low enough, the read noise will be the ultimate limiting factor for sensitivity. However, very low levels of dark current are required to keep the read noise dominant. The requirement for the SW channel is 0.03 e^-/s at a target operating temperature of 6.7 K.

The Arrhenius plot in Figure 4 indicates the challenges of trying to measure dark currents at these levels. For both flavors of detectors, the dark current trend is very clear from 9.2 K down to 7.2 K. Below 7.2 K, we become limited by background photon contamination, either from light leaks into the cold chamber, or by glow from the silicon readout itself. Given the issues we have had with readout glow (see below), we feel this is the likely source of the "plateaus" in the data rather than light leaks. It is encouraging to note that we have achieved consistent measurements of about 0.05 to 0.07 e^-/s at 6 K so that, with care to control the glow, we will be able to test near our very stringent requirements.

4.4 Read Noise

Read noise is the final of the three major sensitivity parameters. Because the SW channel is going to be read noise limited, we desire the performance to be as good as possible. The requirement on the detector is defined to be 19 e^- for a Fowler=8 readout mode. Because other elements in the flight electronics system will contribute somewhat to the overall noise level, the requirement on the whole Focal Plane System is 20 e^-—a root-sum-square of 19 e^- for the detectors and 6 e^- for everything else.

Figure 5 shows the Fowler noise behavior as a function of temperature. The Fowler noise is computed by averaging 8 frames at the beginning of an integration and subtracting that from an average of 8 frames taken at the end of an integration. If the noise is white-noise dominated, the derived value of the Fowler=8 noise should be a factor of two lower than

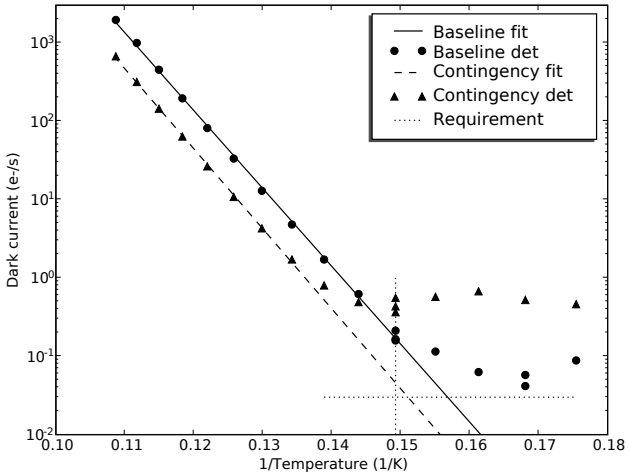

Figure 4. Dark current Arrhenius plots for the two types of MIRI detector layers, measured in flight spare arrays. Both are ultimately limited by the glow from the readout multiplexer. In this case, the contingency array, in spite of having a lower detector dark current, exhibited a higher readout glow.

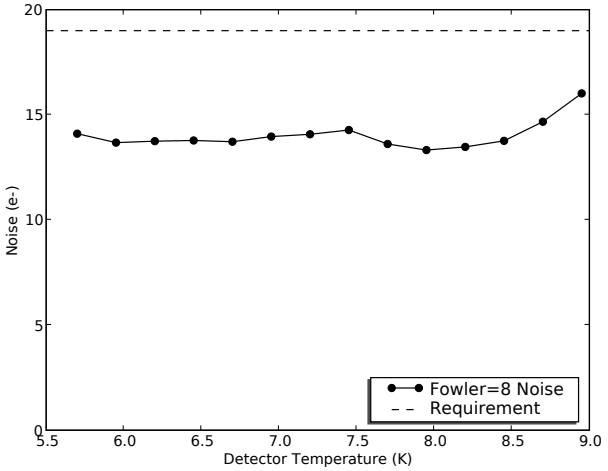

Figure 5. The read noise as a function of temperature. The Fowler=8 noise is derived from the mean difference between two sets of 8 unilluminated frames where the detector bias voltage was set to 0 V. The 14 e^- noise performance is well below the 19 e^- requirement.

the temporal, or frame-to-frame noise, and this is approximately the case. We derived the temporal noise by computing the standard deviation of the value of each pixel sampled a large number of times. For the IC array, this was 26 e^-, while the Fowler=8 noise is about 14 e^-.

We have computed the noise displayed in Figure 5 by setting the detector bias voltage to 0 V; in this way, any dark or photocurrent is eliminated and we will measure only the voltage noise of the readout output amplifiers. We have also performed the experiment by leaving the detector bias at 2 V and looking at the noise in the dark frames. The results are identical until the temperature climbs to ~ 7.5 K. At this point, the shot noise from the dark current begins to dominate the noise, and the total noise begins to exceed the requirement.

4.5 Operability

The MIRI arrays are cosmetically very good. Shown in Figure 6 is an illuminated image from the IC array; the SW and LW spectrometer channels are of similar quality. There are only a handful of obviously dead pixels in the image, and the uniformity of response across the array varies by less than $\pm 3\%$, as measured by using a "flat field" image taken by one detector to correct data taken with a different detector. In the dark integrations (such as seen later in Figure 11), there are also a few hot pixels, though most of the "defects" that are seen are actually cosmic ray hits. All told, each array has fewer than 200 unusable pixels for greater than a 99.9% yield, as can be seen in the bad pixel mask displayed on the right hand side of the figure.

4.6 Well Depth

The well depth of the MIRI detectors is required to be greater than 100,000 e^- to allow a wide dynamic range. For our purposes, the well depth is defined as where the output signal flattens near saturation—*i.e.* where a simple quadratic fit no longer adequately describes the ramp. We can integrate to well over 90% of the saturation level as a result. Assuming an electron-to-DN (data number) conversion ratio of 6 (calculated from the pixel capacitance and signal chain gain), the detectors have a measured well depth of approximately 250,000 e^-, well above the requirement (see Figure 7). We can take advantage of this larger well depth to observe brighter objects for longer integration times, so achieving better sensitivity overlaps with other ground- and space-based instruments.

4.7 Linearity

Related to well depth is the linearity of the output signal. We have found that the output of the MIRI detectors is well described by a simple quadratic equation, so that the linearity is correctable to better than the required 0.25% (see Figure 8).

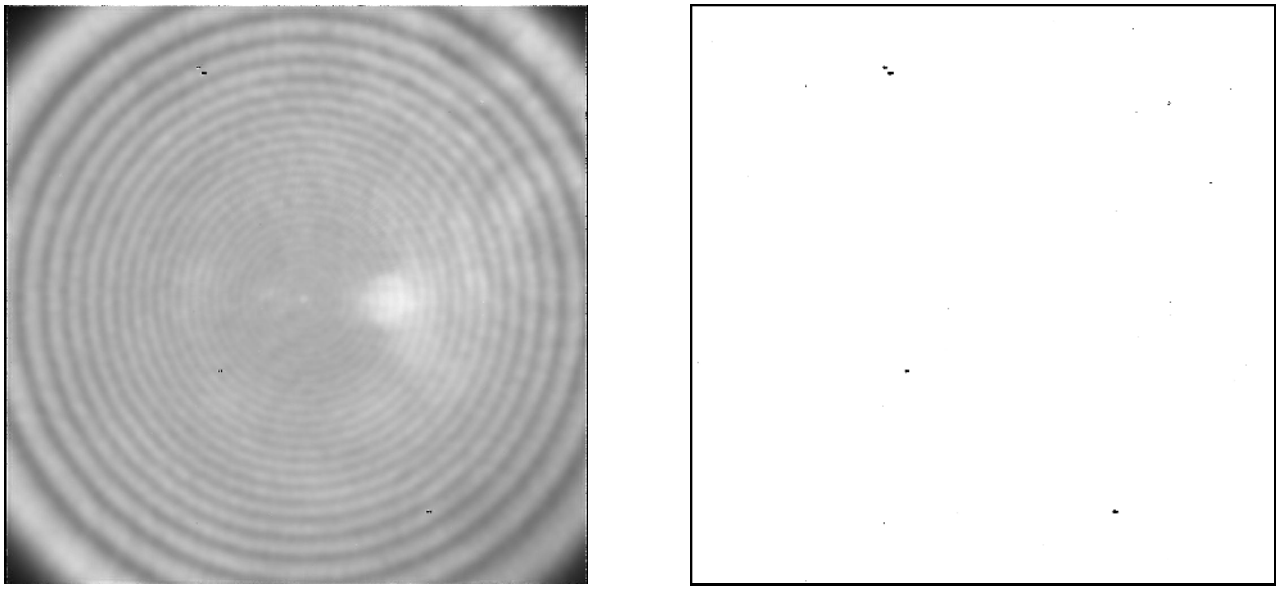

Figure 6. Images showing the operability of the IC detector. On the left is an illuminated IC image showing the good cosmetic quality. On the right is a bad pixel mask generated from the illuminated image, plus additional markers from a dark current sequence.

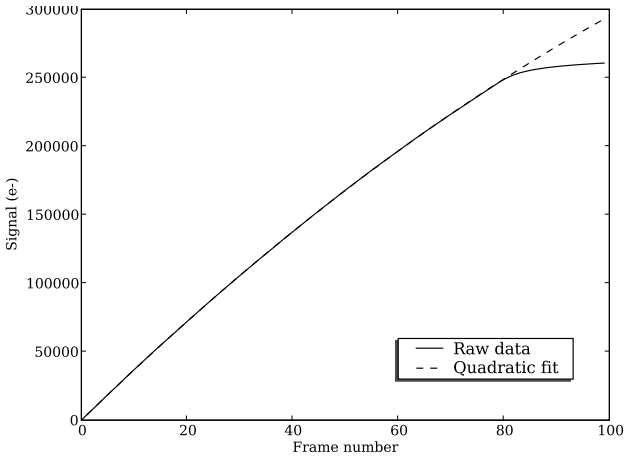

Figure 7. The integrated detector output signal as a function of frame number (2.76 seconds/frame). The ramp is well described by a quadratic fit until hard saturation sets in.

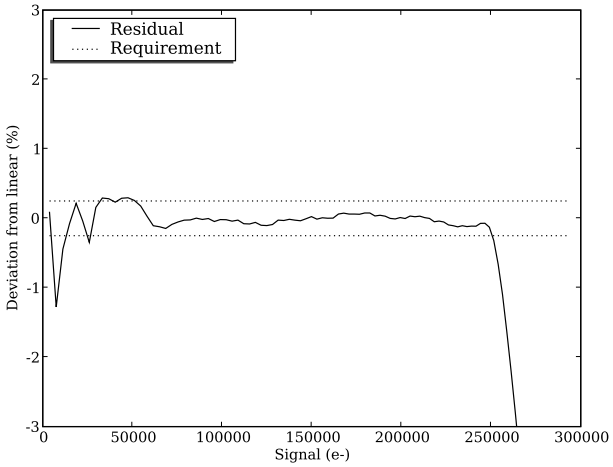

Figure 8. A plot of the residual between an observed integration slope and a quadratic fit to the data. The fit meets the requirement out to an integrated signal of 250,000 e^-.

The linearity appears to be independent of flux level: we typically measure the linearity at 5 or more blackbody settings, and the quadratic terms derived from an integration at one selected flux level can be used to correct the other integrations to that same 0.25% requirement as long as the signal-to-noise ratios are adequate.

4.8 Stability

The stability of the detector is important for the overall calibration of the MIRI data. There are short-term and long-term requirements that the response of the detector (as apart from the drive electronics and other parts of the instrument) varies less than 0.5% in response to a constant illumination source. Figure 9 shows stability data for minute and day timescales. Over a run of 90 minutes, where there were no disturbances of the system, the requirement is easily met.

For the day-to-day variations, the fact that the requirement is still met (in at least these two cases, in a third case the variation was just under 1%) is remarkable given that the detectors are biased and debiased several times over the course

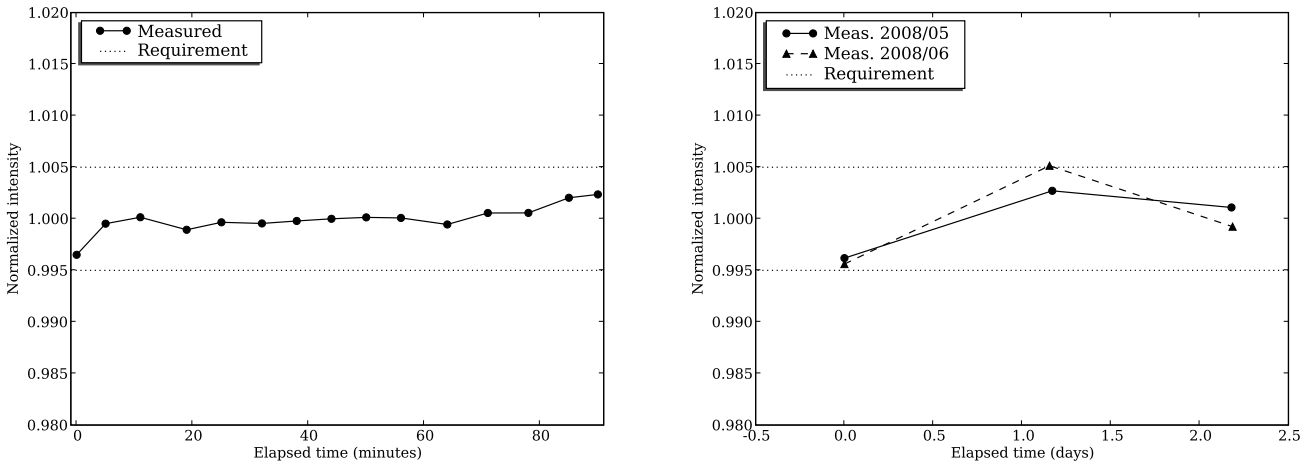

Figure 9. Plots indicating the stability of the detectors to an illuminating source over the course of minutes and days. On the left is a plot of three normalized measurements taken at roughly 5 minute intervals. On the right is the same measurement repeated over the course of 3 days on two separate occasions. (Each set has been normalized to the mean of each set. There is a $\sim 1\%$ decrease between the two sets that is likely to be caused by aging in the blackbody source.)

of a day, the detector temperature is changed over a range from 5.7 to 9.2 K, the blackbody source is turned off, then ramped up in flux. Some or most of the variation must be in the output of the blackbody, rather than in the sensitivity of the detector, so even though the test is only three days long, the fact that consistent results are obtained in the face of huge disturbances bodes well for the stability of the detectors over multi-week timescales.

4.9 Subarrays

An additional method of increasing the dynamic range of the instrument is to read out only a portion of the detector at a rapid rate. This will be especially important for the coronagraph, where we will have to deal with centering bright sources, and with spillover from very bright stars during actual observations. While the MIRI detectors do not have a true windowing function, the shift registers that control the X and Y positions can be arbitrarily reset so "areas of non-interest" may be skipped. The arrays are read from the lower left corner so that, for an arbitrary subarray position, one must reset the array to the origin, step right and up to the beginning of the area-of-interest (AOI), read the first row of interest (a partial row, not the entire row), reset the column shift register to 0, step right to the AOI, read the 2nd partial row, etc. A 256×256 subarray (1/16th of the full array) on the left hand edge takes 1/13.8 of the full frame time (accounting for various overheads), but a subarray on the right hand side will take slightly more than 1/4 of the frame time, because the 768 columns of non-interest on the left side must still be stepped through at the same pixel clock frequency. The MIRI detectors have been oriented within the instrument (with respect to the various optical axes) in order to minimize this overhead for the largest number of cases.

Figure 10 shows four subarray images concatenated vertically and scaled by a factor of 13.8 to match the full frame readout time, versus a full frame image with the same illuminating flux. The areas of overlap are virtually indistinguishable, showing that this subarray readout technique produces high quality data, even if the overhead due to a lack of proper windowing is not optimal.

4.10 Glow

Because MIRI has such stringent dark current requirements, glow from the readout multiplexer becomes painfully obvious, particularly during the 1,000 second integrations expected to make up the bulk of MIRI observations. Both the column and row shift registers have contributed to the observed glow, sometimes at levels of tens of photons/second/pixel. One of the engineering changes that was applied at NASA's request to the mask set while developing the final generation SB-375 multiplexer was the addition of externally-accessible bias lines to control the potential of the *p*-wells in which the *n*-type MOSFETs reside. Careful adjustment of the bias potential on the two types of *p*-wells, one for the row shift registers and one for the output transmission gates, allows minimization of glow associated with forward bias of the *n*-FET substrates. In addition, control of the potentials for the rails of each of the shift register clocks allows more complete glow reduction.

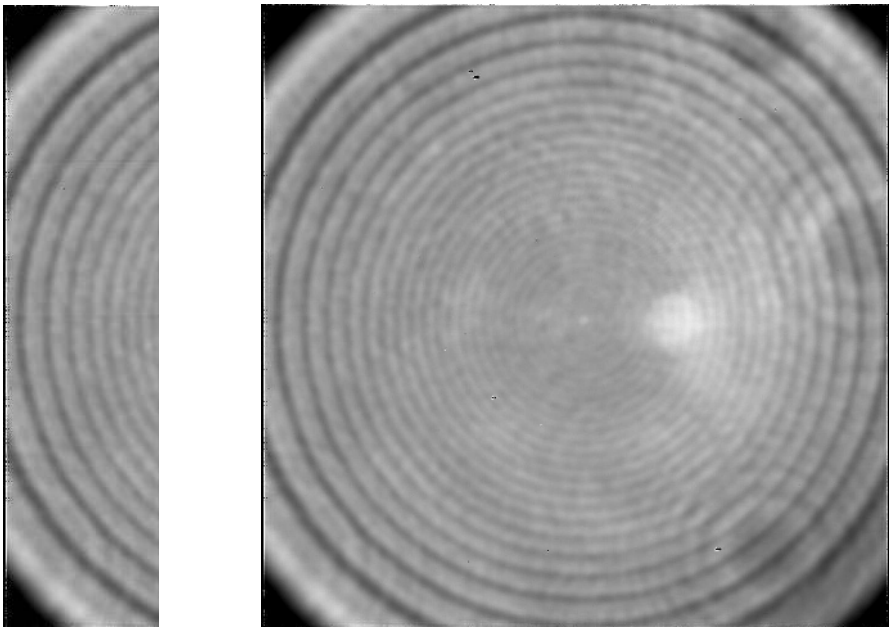

Figure 10. Images obtained by concatenating four 256×256 subarrays that were taken at 4 positions along the left edge of the array (left) vs. an equivalent full frame (1024×1024) image (right). The match in measured fluxes is better than 1% in this case.

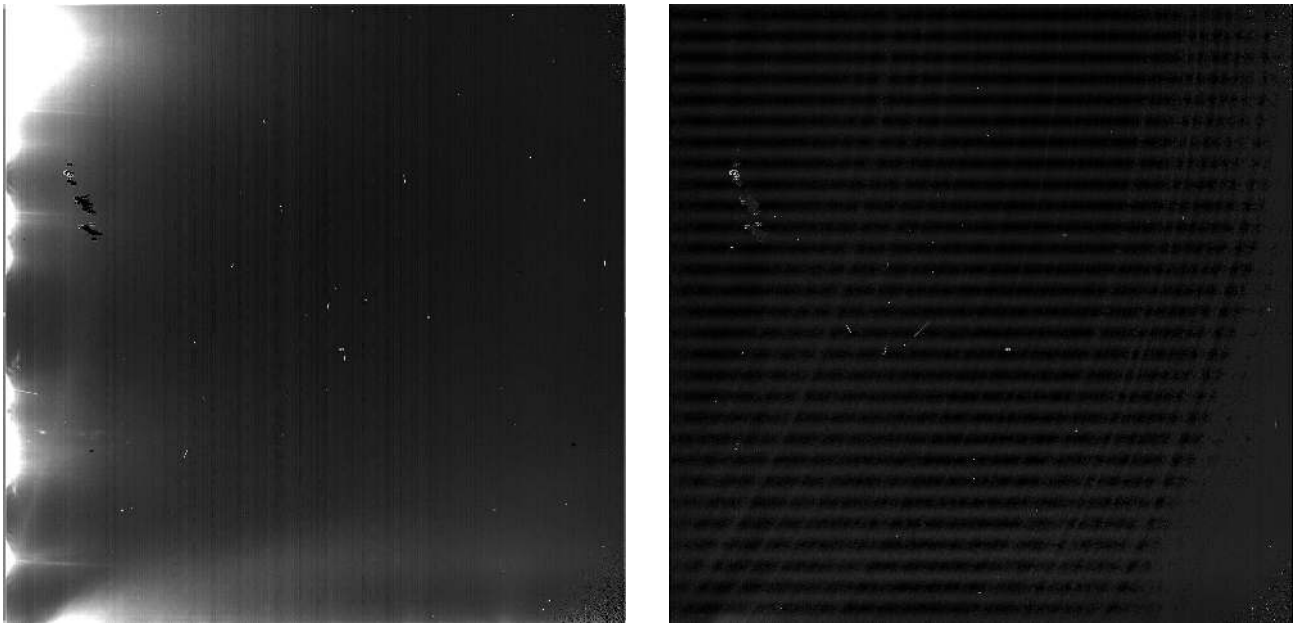

Figure 11. Measured readout glow during the bias voltage optimization, scaled from −1 to 10 e^-/s. The left hand image shows the glow for the default settings; the brightest area in the upper left is about 30 e^-/s/pixel. The right hand image shows the lack of glow (< 0.2 e^-/s/pixel) after both the row and column shift register rails have been tuned.

Figure 11 shows the effect of the glow reduction work, carried on first at NASA/Ames and later confirmed at JPL. The left hand image is the appearance with the default bias voltage values as originally supplied by the manufacturer. Adjustment of the row shift register negative rails eliminated the glow along the left hand edge. An adjustment in the column shift register positive rails away from substrate ground, to a slightly negative potential, virtually eliminates the residual glow along the bottom edge, producing the figure on the right. The glow does appear to be somewhat variable between devices, meaning that the three detectors for MIRI may need to have the biases trimmed individually to ensure optimum dark current performance.

4.11 Reset Signal Droop

We have observed a number of second order "features" of the MIRI detectors during the course of our testing. One of the most pernicious was what we have termed "reset droop", though we recognize other instruments/missions (*e.g.* Spitzer) have used "droop" to describe unrelated read-out effects. This particular effect can be seen in Figure 12. After resetting the detector a number of times (10 frames in this case), we turn off the reset clocks and integrate for a period of time, non-destructively reading the detector at the same rate (2.76 seconds/frame). With the recommended clocking pattern, we noticed that the output would relax and drop to a more negative signal before integrating upward as it should. The presented example shows that it would take ~ 8 frames before the signal would turn around. While we could correct out much of this effect by monitoring and subtracting the values of reference pixels along the edge of the detector, it would be far better to eliminate the effect in the first place.

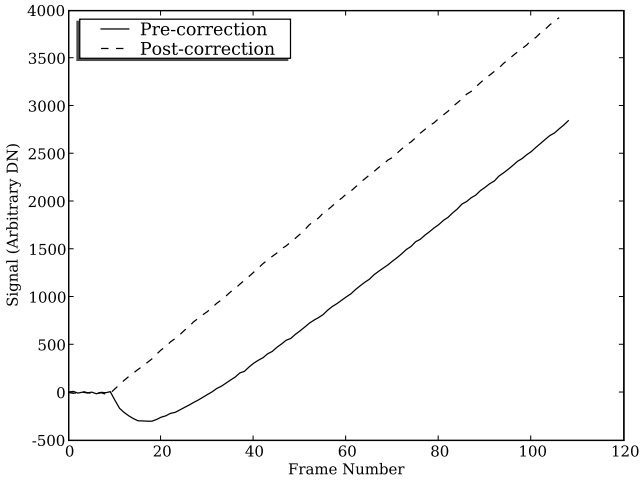

Figure 12. A plot of the signal level vs. frame count for the default clocking pattern (solid line), and for the signal after the change to clocking (dashed line).

The MIRI detectors are reset by connecting a pair of rows of pixels to a reset voltage. This occurs 512 times during a frame readout. It had been recommended that the rows be disconnected from the column bus while the reset pulse was applied. Given that the readouts do not like abrupt changes at this temperature, we decided to change the clocking so as not to perform this disconnection. The result was spectacular. The droop disappeared entirely and now shows textbook behavior. We have not observed any change in the data quality or power dissipation, so, at least for the MIRI detectors, this disconnection is not desirable.

4.12 Slew Rate Ghosts

"Ghosting" is a term we have used when the readout outputs are not able to slew fast enough from a fully (or nearly) saturated pixel to a neighboring dark pixel. Because MIRI's detectors have four data outputs that address adjacent columns (as opposed to quadrants), the "ghost" will appear four pixels to the right of a saturated pixel in the final image. This ghosting appeared more strongly than we expected with the default biases, but it can be reduced by altering the drive current through the output amplifiers, both by a change in the source voltage and in the load resistor (see Figure 13). There is a net impact on the power dissipation of the array (faster drive = higher power), but the necessary increases have not yet exceeded the power allocation of the arrays.

4.13 Latent Images

We do not currently have the capability in our test dewars at JPL to place point source illumination on the flight detectors. However, we do have some data concerning latent images—after-effects of bright and/or saturated sources—from engineering tests done on the MIRI Verification Model. The tests and results are described more extensively in [10], but the basic result is shown in Figure 14 for completeness and we expect the flight arrays to have essentially identical behavior. In this test, a nearly-saturating source was placed on the array, then removed for the following integration. The center of the "star" was depressed by about 5,000 e^- in the raw frames but, in the slope-fit processed image, the deviation from the

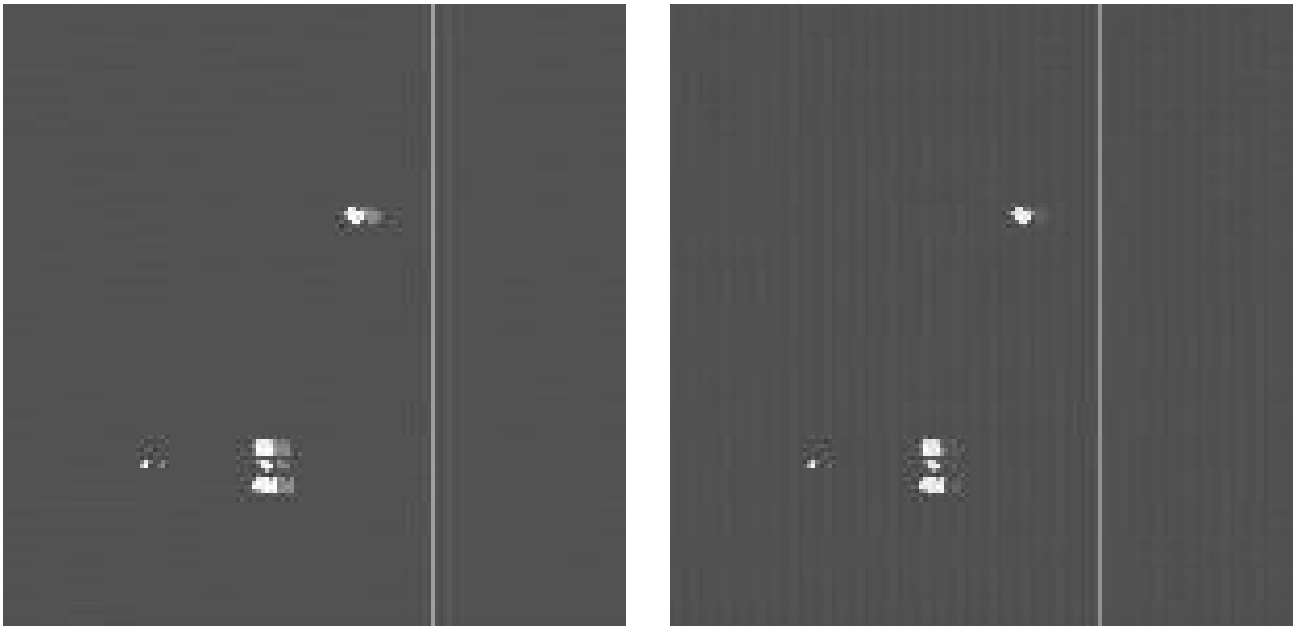

Figure 13. “Ghosts” due to slew rate effects in the output amplifiers. On the left is part of an image taken when the output drive current severely limits the slew rate. Each of the bad pixels and the bad column have a “ghost” four pixels to the right. (There are four outputs, so the next pixel in a given output will appear four pixels later). The right hand image shows the effect with greatly increased drive current. The ghosts of the very worst pixels are still present, though much reduced, but the weaker bad pixels and the bad column ghosts are entirely gone.

Figure 14. A latent image of a “star” found during the engineering instrument testing. The saturating point source image is shown on the left. The latent appears to affect only the offset of the starting signal level of the integration as shown in the right hand image—the measured affect on the slope is very small, less than a few electrons per second.

surrounding pixels was only 3 e^-/s, negligible for many of the cases MIRI will deal with, and should be manageable for most of the rest. The main concern is for the coronagraph, where we will be searching for faint spots around very bright sources, and our ability to dither or make alternate observations is limited.

4.14 Other Cosmetic Issues

There are a number of other cosmetic features seen in the MIRI detector data. For those familiar with the Spitzer/IRAC instrument behavior, most of the features seen there (column droop, jail-bar patterns, etc.) will be represented in MIRI. Two are presented in Figure 15. The column effects in the left image, where the level of an entire column containing a bad pixel is pulled down, are very similar to effects seen in Spitzer data. The image on the right shows a tree ring pattern seen as a small intensity offset (~ 0.2 e^-/s). The pattern is related to the original location of the die on the detector wafers before it is diced out; we have confirmed this by matching the direction of the tree rings with the detector die identifier. It is likely caused by swirl dislocations in the crystalline structure of the silicon boule from which the detector wafers were cut. The effect on the data is negligible; the pattern is constant and can be removed by subtracting another dark current frame from the image.

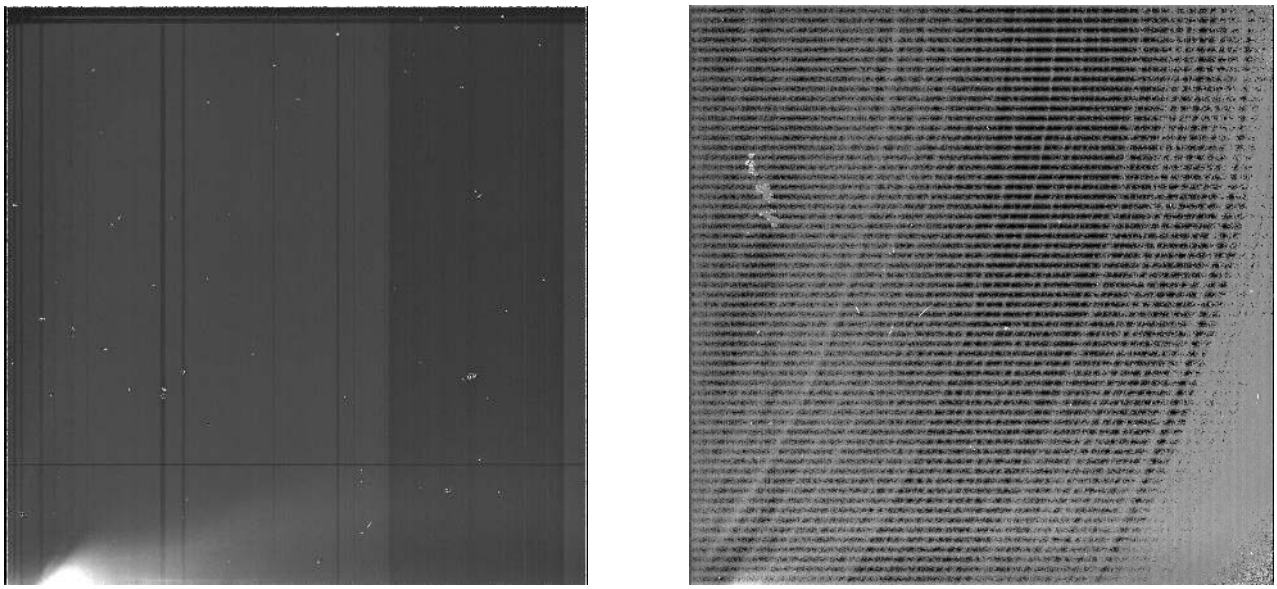

Figure 15. A few miscellaneous cosmetic issues. On the left is a dark frame image, scaled from -1 to 5 e^-/s, that shows column depressions caused by bad (shorted) pixels. This pattern is not always seen, even on the same array—subsequent cooldowns showed no similar effect with this device. On the right is an effect we call "tree rings" (the faint quarter circle pattern centered on the upper left corner); this is a slope-fit image, with the intensity highly exaggerated (-2 to 2 e^-/s). It is associated with the location on the detector wafer from where the particular die came; it is primarily a small offset effect—it does not affect the overall response uniformity.

5. SUMMARY

The MIRI flight and spare SCAs have been selected and are proceeding into the next stage of integration into the Focal Plane Modules. Testing of the SCAs has shown that they are of very high quality and will enable MIRI to meet all its sensitivity requirements, especially when they are chosen and optimized for each of the three optical channels in the instrument.

There have been a number of operational issues related to clock patterns and bias voltages that have required intensive investigation such as reset droop, multiplexer glow, slew rate ghosting, etc., but the most troublesome of these have now been solved and will be eliminated in the flight instrument. The general behavior of the arrays is now good enough that we are able to concentrate on the smaller effects that we will have to live with, but for which we will need to do thorough characterizations, such as latent images, etc.

ACKNOWLEDGMENTS

All this work would have been impossible if we could not have stood on the shoulders of those people, instruments, and missions using Si:As IBC detectors that have gone before us. In particular, we are indebted to Craig McCreight for leading the development of megapixel-class Si:As detectors in the days after Spitzer, but before MIRI, and for his help in early testing of our engineering devices at Ames. Craig McMurtry at the University of Rochester also provided much help during the engineering phase to help understand the behavior of the readouts and begin the optimization process. Alan Hoffman and Peter Love led the charge in developing the MIRI arrays at RVS before their retirements, and it is thanks to their insight, care, and willingness to take a few calculated risks that we have such fine detectors to work with today. Finally, thanks to Analyn Schneider and Johnny Melendez of JPL who put in untold numbers of hours supporting the data taking summarized here.

The research described in this paper was carried out at the Jet Propulsion Laboratory, California Institute of Technology, under a contract with the National Aeronautics and Space Administration.

REFERENCES

[1] Wright, G., Rieke, G., and et al., "The JWST MIRI instrument concept," in [*Optical, Infrared, and Millimeter Space Telescopes*], Mather, J., ed., *Proc. SPIE* **5487**, 653–663 (2004).

[2] Wright, G., Rieke, G., and et al., "Design and development of MIRI, the mid-IR instrument for JWST," in [*Space Telescopes and Instrumentation I: Optical, Infrared, and Millimeter Wave 2008*], *Proc. SPIE*, these proceedings (2008).

[3] Sukhatme, K., Thelen, M. P., Cho, H., and Ressler, M., "Development of a focal plane module for JWST/MIRI," in [*High Energy, Optical, and Infrared Detectors for Astronomy III*], *Proc. SPIE*, these proceedings (2008).

[4] McMurray, R., Johnson, R., McCreight, C., and et al., "Si:As array performance for SIRTF/IRAC," in [*Infrared Spaceborne Remote Sensing VIII*], M. Strojnik, B. A., ed., *Proc. SPIE* **4131**, 62–69 (2000).

[5] Ennico, K., McKelvey, M., McCreight, C., and et al., "Large format Si:As IBC array performance for NGST and future IR space telescope applications," in [*IR Space Telescopes and Instruments*], Mather, J., ed., *Proc. SPIE* **4850**, 890–901 (2003).

[6] Love, P., Beuville, E., Corrales, E., and et al., "1024 x 1024 Si:As IBC detector arrays for mid-IR astronomy," in [*High Energy, Optical, and Infrared Detectors for Astronomy II*], Dorn, D., ed., *Proc. SPIE* **6276**, 62761Y (2006).

[7] Garnett, J. and Forrest, W., "Multiply sampled read limited and background limited noise performance," in [*SPIE Infrared Detectors & Instrumentation*], Fowler, A., ed., *Proc. SPIE* **1946**, 395–404 (1993).

[8] Stetson, S. B., Reynolds, D. B., Stapelbroek, M. G., and Stermer, R. L., "Design and performance of blocked-impurity-band detector focal plane arrays," in [*Infrared Detectors, Sensors, and Focal Plane Arrays*], Nakamura, H., ed., *Proc. SPIE* **686**, 48–65 (1986).

[9] Herter, T., "IBC arrays: Present and future prospects," in [*Infrared Astronomy With Arrays: The Next Generation*], McClean, I., ed., 409–417 (1994).

[10] Lim, T., Grundy, T., and et al., "First results from MIRI verification model testing," in [*Space Telescopes and Instrumentation I: Optical, Infrared, and Millimeter Wave 2008*], *Proc. SPIE*, these proceedings (2008).